

Influence of Slip Localization on Crack Initiation at the Grain Scale

M. Sauzay

CEA Saclay, DEN-DMN-SRMA, Gif-sur-Yvette, France

1. Introduction

Slip localization occurring at the grain scale has been extensively observed, particularly in faced-centred cubic (FCC) metals and alloys subjected to either post-irradiation tensile tests (channelling) [1-4] or cyclic loadings (persistent slip band (PSB) formation) [5-10]. Plastic slip is localized in thin slip bands. The degree of localization seems to be high. It could be evaluated using the ratio between the slip band and macroscopic axial plastic strains. Following the atomic force microscopy (AFM) measurements of Was et al. [3], this ratio is equal to about 10 for austenitic steels subjected to post-irradiation tensile loading (macroscopic axial strain of 0.03). The transmission electron microscopy (TEM) observations of Sharp [1] and Edwards et al. [2] concerning either single crystals or polycrystals of copper subjected to post-irradiation tensile loading allowed the evaluation of channel plastic slips. The obtained localization degrees seem to be about ten too. Following the AFM study of Wejdemann and Pedersen [10], the PSB's plastic strain is about fifty times higher than the macroscopic plastic strain.

At least two main mechanisms explain slip localization. The first mechanism is valuable for post-irradiation tensile tests carried out on FCC metals and alloys. It is based on interactions between mobile dislocations and irradiation-induced defects. Irradiation induces atom displacement and defect formation (interstitial Frank-loops in austenitic stainless steels [11], stacking fault tetrahedral in copper [2]). During post-irradiation deformation, complex reactions occur between gliding dislocations which can lead to the removing of irradiation defects, producing finally thin defect-free channels [1,2,11]. Cycling of precipitation-hardened alloys induces thin slip band formation if precipitates are shearable [12]. The second mechanism corresponds to (ductile) FCC polycrystals subjected to cyclic loadings. PBSs are often made of hard walls (high density of edge dislocation dipoles) and soft channels (low density of screw dislocations which glide and cross-slip). This corresponds to the well-known ladder-like structure [5-9]. In low stacking-fault energy (SFE) metals and alloys, PSBs appear as well [10] even if the ladder-like structure is not observed.

Several computations have been reported in the literature aiming to evaluate the plastic slips inside PSBs. They were first modelled as elongated bulk inclusions embedded in a matrix which mimics the whole polycrystal [13]. This permitted the use of the analytical solutions given by Eshelby for bulk inclusions [14]. Secondly, finite element (FE) computations using crystalline plasticity allowed the study of surface effects [15-17]. In the case of type B surface slip bands (glide through the free surface), both slip magnitude and heterogeneity are considerably increased by surface effects [16,17].

Channels and PSBs impinge at grain boundaries (GBs). This induces stress or plastic strain concentrations as shown by TEM observations on copper polycrystals deformed after neutron irradiation [2]. Edwards et al. observed either local lattice rotations corresponding to high elastic strain concentrations or considerable amount of (plastic) shearing at the GB if another channel formed on the opposite side of the grain boundary [2]. Because of these interactions with GBs, channels and PSBs are often considered as promoting GB crack initiation and propagation. Corresponding crack initiation mechanisms were investigated experimentally for copper [18] and nickel [19] subjected to cyclic loadings. Concerning irradiation assisted stress corrosion cracking (IASCC), channeling is considered as promoting GB crack initiation as well [20,21,2] even if other mechanisms are influent (corrosion, radiation induced segregation (RIS) [22]).

Concerning modelling in the continuous framework, several studies have been dedicated to the evaluation of GB stress concentrations. Margolin and co-workers deduced from optical observations of slip traces that stresses are higher close to the GBs [23]. Neumann highlighted the effect of crystalline elasticity on stress concentration at GBs [24]. Recently, Diard et al. used large-scale Finite Element computations for evaluating stress gradients in the vicinity of GBs, induced by plastic deformation incompatibilities [25]. These studies highlighted stress concentrations which could promote GB crack initiation. Concerning specifically the influence of slip band impingement, stress concentrations have been evaluated analytically considering discrete dislocation pile-ups. The local tensile stress acting on the leading dislocation of the pile-up was computed. For brittle fracture occurrence, this should be higher than a the cohesion stress, which depends on the surface and grain boundary energies [26,18]. A similar approach, but based on an energy criterion, was followed by Tanaka and Mura [27]. These discrete dislocation models assumed that slip was localized on particular slip planes, for example along the interfaces between the slip bands and the grain. Nevertheless, some observations show that a non-negligible fraction of slip occurs homogeneously inside the PSBs (cf interferometry measurements [6], in-situ TEM observations [28] and AFM measurements [3,10]). The observations of Jiao et al. [3] and Byun et al. [4] on post-irradiation deformed 316L steel showed that shear strain is uniformly distributed through the thickness of channels.

This work is dedicated to a numerical evaluation of surface strain and GB stress concentration induced by strain localization using a continuum approach. The influence of localization on particular fracture mechanisms (oxide layer fracture, grain boundary cavity nucleation and fracture) is then discussed.

2. Modelling hypothesis

2.1 Modeled microstructures

One slip band, modelling either a channel or a PSB, is embedded at the free surface of a matrix which mimics the whole polycrystal (Fig. 1 a) and b)). The length and thickness of the channel are denoted as L and h . The length L is close to the grain size, as shown by TEM observations. The ratio between L and h is

generally high (about hundred or even more for large grain sizes). Following observations carried out in the small strain regime [29], grains containing channels are often well-oriented (high Schmid factor values). As observed by Byun et al. [4], channels are parallel to one easy slip plane. For FCC polycrystals, 12 easy slip systems, (n_i, m_i) $i=1, \dots, 12$, are defined in each grain. The unit normal vector of the i^{th} slip system is denoted as n_i whereas the unit slip vector is denoted as m_i . For FCC metals, the slip systems are defined by normal directions $\{111\}$ and slip directions $\langle 110 \rangle$. The well-oriented grains present one particular slip system (n, m) with a Schmid factor equal to its maximal value, 0.5. The resolved shear stress is defined as the maximum shear stress magnitude among those computed on each easy slip system of the considered grain, $|\tau_i| = |m_i^T \Sigma n_i|$ ($i=1, \dots, 12$). The local and macroscopic stress tensors are denoted as σ and Σ . The Schmid factor is the ratio between the local resolved shear stress and the remote axial stress, Σ_{xx} (tensile axis, x). For the well-oriented grains, both the n and m slip vectors are inclined at 45° with respect to the tensile direction. Among all possible well-oriented slip planes, type B facets lead to the highest surface slips due to the lack of constrain effect following FE evaluations [16]. Both vectors are inclined at 45° with respect to the free surface.

Another configuration takes into account two parallel slip bands instead of only one. TEM observations show that several parallel slip bands are usually observed in the same grain, even in the small strain regime [2,3,8-10,13]. In our study, the inter-bands spacing varies between 0.7 and $3\mu\text{m}$, which are distances usually reported in the literature. The influence of parallel slip bands could then be investigated. Finally, a more complicated mesh was built for investigating the influence of the orientations of the neighbour grains which have been meshed.

For studying the aspect ratio effect various values of L/h are used: from $L/h=200$ ($L=10\mu\text{m}$ and $h=50\text{nm}$, which are suitable values for the 316L steel pre-irradiated at doses higher than a few displacements per atom (dpa) and then deformed [4,11]) and $L/h=15$ (PSBs in FCC polycrystals which grain size is about $10\mu\text{m}$).

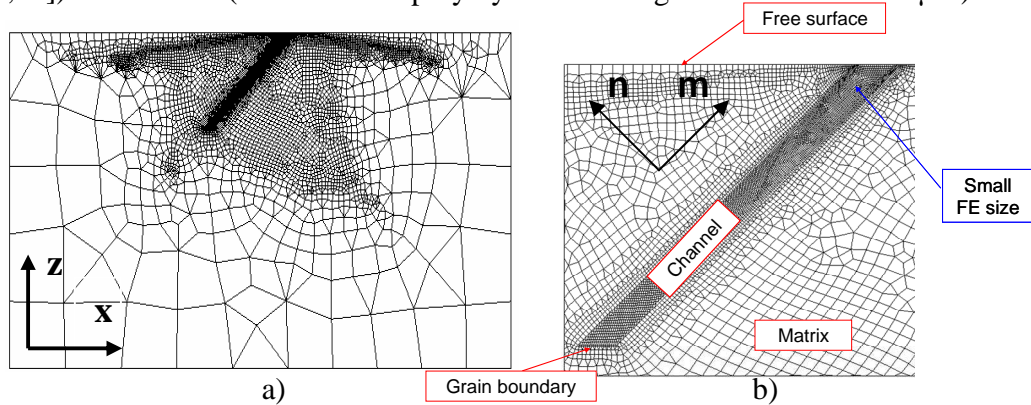


Fig. 1. a) Zoom on the mesh of the matrix containing the surface slip band (loading axis, x); b) zoom of the surface slip band. Slip vectors: n , m (well-oriented slip system).

2.2 Crystalline constitutive laws

Both slip bands and matrix obey isotropic elasticity. The shear modulus and Poisson ratio are denoted as μ and ν , and the values have been taken from [30]. As usual, constitutive crystalline viscoplasticity laws are defined by the viscoplastic flow equation and the hardening equation (see for example [31]). The viscoplastic flow law gives the dependence of the viscoplastic slip rate (i^{th} slip system), $d\gamma_i^{\text{vp}}/dt$, with respect to the corresponding shear stress, τ_i . The hardening equation allows the computation of the evolution of the critical resolved shear stress (CRSS) on the i^{th} slip system, $\tau_{c,i}$, depending on all the viscoplastic slip rates ($j=1,2$). Self-hardening ($j=i$) and latent hardening ($j \neq i$) are taken into account through the parameter q ($q > 1$). The equations used in this work are similar to the ones proposed by Anand et al. [31].

Because of the high value of the chosen exponent of the Norton law, $n \approx 50$, strain-rate effect is neglected following mechanical tests for austenitic steels [32,33].

The influence of the initial CRSS of each considered “phase” (the matrix is a “hard” phase and the slip band is a “soft” phase) is investigated based on values given in the literature. The soft phase is considered first. The TEM observations indicated that channels are quite free of defects. In addition, the dislocation densities are rather weak. That is why the initial critical shear stresses of single crystals without defects have been used as initial values for the channels. For example, for 316L austenitic stainless steels values of about 33MPa and 40MPa have been given by Li and Laird [34] and Gorlier [35], respectively, using mechanical testing of well-oriented, recovered, single crystals at room temperature. Secondly, the initial CRSS of the irradiation defect-full hard phase is evaluated referring to theoretical approaches reported in the literature and evaluating the critical shear stress for allowing a mobile dislocation to overcome the irradiation defects obstructing dislocation glide. Bacon and Osetsky used the Orowan formula [36]. Using typical values of high dose neutron irradiation (40 displacements per atom (dpa)), i.e. Frank loop diameter: 7nm and density: $6 \cdot 10^{23}/\text{m}^3$ [38], a typical critical shear stress of about 360MPa is calculated. Using the same experimental data, the application of the forest model proposed by Pokor et al. [37] gives a critical shear stress of about 200MPa. Finally, the molecular dynamics computations of Nogaret et al. gave a range of 300-600MPa for the shear stress required for unfaulting of Frank loops in 316L at 300°C [38]. For being general enough, three different critical shear stresses are used in the hard phase of pre-irradiated austenitic steels: 300, 500 and 1000MPa. Concerning localization induced by cyclic loadings, the PSB CRSS is supposed to be equal to the PSB threshold i.e. the plateau shear stress measured during cyclic tests carried out on well-oriented single crystals (copper: 28MPa [5,6], nickel: 50MPa [7] at room temperature). The matrix around the PSB is supposed to be elastic.

The hardening mechanisms seem weak in the channels of irradiated metals and alloys, as during stage I of tensile deformation of 316L well-oriented single crystals [34,35]. Irradiation defects have been removed and are not compensated by dislocation multiplication. A hardening slope of about 1MPa per % of plastic slip is used. It is due to short-range interactions, because long-range interactions are intrinsically taken into account in the FE computations (back-stresses induced

by the surrounding hard grain and matrix). Finally, two extreme cases will be considered for studying the effect of the latent hardening coefficient, q . A small value, $q=1.4$ [31], is used to simulate material behaviour for which the activation of new slip systems during tensile loading is easy and multiple slip is favoured, which is typical of a high SFE material. The use of a very high value, $q=1400$, hinders the activation of secondary slip system, which is typical of a low SFE material. This allows the study of the effect of multiple slip versus planar slip.

2.3 Finite Element computations

The FE code Cast3m [39] is used. Additional subroutines for integrating crystalline viscoplasticity laws based on the work of Héraud [34] have been used recently for studying the influence of crystalline elasticity on the resolved shear stress distribution at the free surface of multicrystals [40,41]. Whatever the modelled configuration, the matrix is at least ten times larger than the channel length, L . For building the 3D meshes, 2D meshes (Fig. 1 a)) are extruded along the y axis (Fig. 1 a)). The meshes are built with tetrahedra. Both plane stress and plane strain conditions are used (depending on the free stress or imposed displacements applied to the two surfaces parallel to Fig. 1 a)). The results depend weakly on the plane stress / plane strain condition and mesh width (along the y axis) because glide mainly occurs parallel to the (xz) plane (Fig. 1 b)). The influence of FE size and time increment on surface slips is weak (relative error smaller than 5%). Uniform horizontal uniaxial displacements are prescribed along the x axis, at one matrix lateral face (perpendicular to tensile axis, x). The maximum total remote strain is small enough for avoiding macroscopic yielding.

3. Computation of surface and grain boundary slips

Whatever the applied load, the primary slip is higher in the vicinity of the free surface (Fig. 2 a)) than in the bulk of the slip band. It is defined as the ratio between the displacement along the most active Bürgers vector and the slip band thickness, h . The slip in the vicinity of the grain boundary is much smaller than at the free surface (Fig. 2b)). This difference is due to the constrain effect induced by the hard material surrounding the grain boundary. The higher the matrix CRSS, the higher the free surface effect (Fig. 2 b)). The matrix CRSS affects strongly the slips until a saturation regime is reached. On the contrary, the slip band CRSS affects weakly the slip values provided it is much lower than the matrix CRSS (a few ten MPa versus a few hundred MPa). As shown in Fig. 2 b), slip planarity ($q=1400$) affects only weakly the surface slip values. Either a few slip systems are activated (typically two ones for $q=1.4$) or only one ($q=1400$), but the resulting surface step is quite the same.

The slip computed by the FE method is now compared with the analytical formula proposed in [16] with $r_{surface}=1.9$, and $\tau_{c,SB}$ denoting the slip band CRSS:

$$\gamma^p = r_{surface} (1 - \nu) \frac{L}{h} \left(1 + \frac{h}{L} \right)^2 \frac{0.5 \Sigma_{xx} - \tau_{c,SB}}{\mu} \quad (1)$$

Various materials (matrix and slip band CRSS and aspect ratio) and loads are

considered (channelling in pre-irradiated 316L steel using various L/h values, PSBs in copper and nickel polycrystals, A286 austenitic steel containing shearable precipitates). Following Fig. 3 a), the agreement is generally satisfying. This allows easy evaluation of surface slips for type B slip bands.

Finally, the influence of microstructure is shortly studied (Fig. 3 b). Provided the inter-channel distance is higher than the slip band thickness, another parallel channel leads to only a weak increase of surface slip. The influence of the crystallographic orientations of the neighbour grains is stronger. The relative amplitude induced by the random orientations is higher than $\pm 30\%$ (Fig. 3 b)). This amplitude is obtained using only these two extremum configurations, chosen following the orientations between the neighbour grains such as the tensile axis is either a $\langle 100 \rangle$ or a $\langle 111 \rangle$ axis (Fig. 8 of [40]). Considering austenite crystalline elasticity, the ratio between the $\langle 100 \rangle$ and $\langle 111 \rangle$ Young's moduli is about 3 [40].

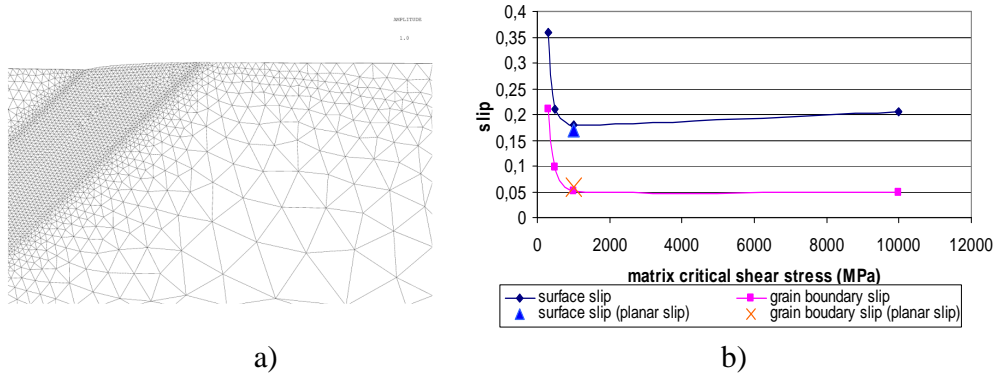


Fig. 2. Deformation-induced surface relief of the channel (magnitude *1); b) Influence of the matrix critical shear stress and planar/multiple slip character on surface and grain boundary slips. Pre-irradiated 316L austenitic stainless steel. Channel CRSS: $\tau_{c,channel}=50\text{MPa}$. Latent hardening coefficient: $q=1.4/1400$. Plane stress. Macroscopic axial stress: $\Sigma=780\text{MPa}$, macroscopic axial strain: $E=0.45\%$. Channel/matrix mesh, $L/h=15$.

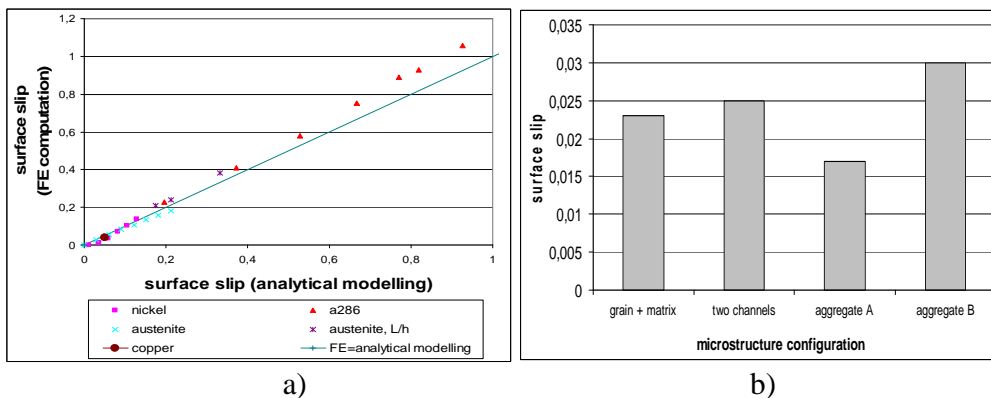


Fig. 3. a) Plot of the surface slips computed by FE for different materials and loading conditions as a function of the surface slips computed using the analytical formula (Eq. (1)). Austenitic stainless steel, nickel, copper (see the text for details about the material and microstructure parameters). Slip band / matrix mesh; b) effect of the neighbouring microstructure (additional slip band or neighbouring grain) on surface slip.

grains with particular orientations). Austenitic stainless steel, 300°C, $\tau_{c,matrix}=500\text{MPa}$, $\tau_{c,channel}=33\text{MPa}$, $\Sigma=200\text{MPa}$. Slip band aspect ratio: $L/h=15$.

4. Influence of slip localization on crack initiation at the grain scale

During tensile/cyclic loading in water/air environment, a passive oxide layer forms on the surface of the many specimens, offering some protection from further oxidation. If this oxide layer is fractured as a consequence of deformation in the underlying polycrystal, the passivation is lost locally, and re-oxidation occurs. The process of repeated fracture and re-oxidation is the central principle of the slip-oxidation models [42]. The oxide brittle fracture strain is denoted as $\varepsilon_{f,oxide}$. The surface slip band strain, $\varepsilon_{xx,SB}$, is about one-half of the plastic slip, γ^p , (the slip vectors form an angle of 45° with respect to the tensile axis, x .) If the macroscopic behaviour is elastic, the macroscopic axial strain can be easily evaluated by $E_{xx}=\Sigma_{xx}/Y$, where Y is the Young's modulus. The time required for oxide fracture is equal to $\varepsilon_{f,oxide} / (dE_{xx}/dt)$ if localization is neglected and $\varepsilon_{f,oxide} / (d\varepsilon_{xx,SB}/dt)$ if not. Following Eq. (1), the slip band plastic slip and axial strain vary quite linearly with respect to the applied strain, E_{xx} . If the tests are strain-controlled, then the ratio of the required oxide fracture times without and with localization is equal to $(\varepsilon_{xx,SB}/E_{xx})$, which is plotted in Fig. 4 a) (exponent: $m=1$). As expected, it is proportional to the slip band aspect ratio, L/h . If this one is higher than 200, the oxide fracture takes place a few hundred earlier with localization than without. Following [42], the short crack propagation rate, da/dt , is proportional to either $((dE_{xx}/dt) / \varepsilon_{f,oxide})^m$ or $((d\varepsilon_{xx,SB}/dt) / \varepsilon_{f,oxide})^m$, with m the exponent of the decay of the current density at each repeated oxide fracture and re-oxidation of the bare surface. In the case of strain-controlled tests, the ratio of crack propagation rates without and with localization is equal to $(\varepsilon_{xx,SB}/E_{xx})^m$. Following [42], the values of m belong to the range 0.3-1, depending on the material and environment conditions. The values computed for these exponent values are plotted in Fig. 4 a). If the m value is high (~ 0.8), the crack propagation rate is multiplied by a few hundred for a slip band aspect ratio of $L/h \geq 200$. But if the m value is very low (~ 0.3), then the crack propagation rate is only increased by a factor of 5 to 10. Slip computations do not take into account the influence of the oxide layer on the mechanical point of view. Following the FE study of the effect of an oxide layer above a slip band embedded in a matrix [17], the band surface slip would be about one-half smaller if the material surface had an oxide layer having a thickness equal to the slip band thickness. But the localized axial strain would nevertheless be much higher than the macroscopic axial strain.

The stress iso-value plots show that slip band impingement at grain boundaries (GBs) induces high stress concentrations close to GBs (Fig. 4 b)). Considering irradiation and loading conditions, and a typical value of channel aspect ratio of 200 (channel thickness: $h \sim 50\text{nm}$ and grain size: $L \sim 10\mu\text{m}$), the normal stress at the GB perpendicular to the loading axis is 8 times higher than the remote stress if the distance to the channel is smaller than one tenth of the channel thickness, h . It is 4 times higher provided the distance is smaller than one half of the thickness. The stress fields computed for aspect ratios of either 15 or 200 show that the higher

the aspect ratio, the higher the stress concentration. Stress triaxiality, defined as the ratio between the pressure and the von Misès stress, is considerably increased close to the GB (about three times higher than the macroscopic one if the distance to the channel is smaller than one tenth of the channel thickness). Computations using a finer mesh size close to the GB show that the maximum stress depends a little on the mesh size (relative variation of about 25%), even if the grain boundary slip does not. The TEM observations of Edwards on irradiated pure copper show that local lattice rotations arise at the intersections of channels/twins and grain boundaries [2], which they link to local stress concentrations.

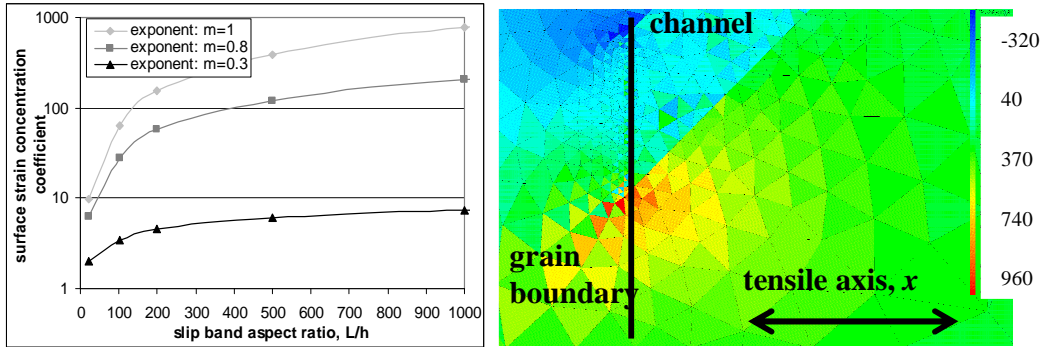


Fig. 4. a) Slip band concentration coefficient due to slip localization, $(\epsilon_{xx,SB}/E_{xx})^m$, depending on the slip band aspect ratio, L/h . For $m=1$, this corresponds to the strain/time to oxide crack initiation concentration coefficient and for $0.3 < m < 0.8$ to the short crack propagation rate (m : exponent of the decay of the oxidation current density) [42]; b) Isovalues of the stress normal to the grain boundary, σ_{xx} (MPa). Irradiated 316L steel, $\tau_{c,channel}=30\text{MPa}$, $\tau_{c,matrix}=300\text{MPa}$, 300°C , $L/h=200$, applied tensile stress: $\Sigma_{xx}=120\text{MPa}$.

Local stress concentrations should accelerate grain boundary crack initiation when diffusion processes are active. Diffusion of oxygen or hydrogen may occur along grain boundaries, most likely along general grain boundaries. This would decrease the grain boundary cohesion strength and fracture energy. Following the molecular dynamics computations of Van der Ven and Ceder [43], a fraction of 40% of oxygen atoms in a $\{111\}$ aluminium plane induces a relative decrease of a factor of two in the cohesion strength. The same fraction of hydrogen atoms induces a decrease of a factor three. As at distance of one-tenth of the channel thickness, the GB normal stress is about 8 times higher than the applied stress (equal to the yield stress). For high irradiation dose and 316L steel, the yield stress is about 800-1100MPa [4,22]. Therefore, the GB stress is higher than 6000MPa whereas the theoretical cleavage stress is about $Y/10$, that is 17000MPa [30]. If oxygen/hydrogen diffusion is taken into account, the GB cohesion strength could be reached along a segment of GB of about one tenth of the channel thickness.

Nevertheless, several experimental studies have shown that an environment effect is not necessary for obtaining intergranular damage during slow strain rate tensile loading of pre-irradiated austenitic stainless steels (see the results of the tests in

290°C inert gas of Onchi et al. [44] and in 340°C argon of Toivonen et al. [21]). Further, Lim and Raj observed cavitation at (general) GBs in pure (unirradiated) nickel polycrystals in vacuum (10^{-5} Pa) at 300°C, reportedly induced by slip band impingement during cyclic tests [8]. On the one hand, RIS could affect the GB cohesion strength in case of pre-irradiation. On the other hand, cavitation could occur because of GB stress concentration and diffusion of vacancies along general GBs, which is accelerated with respect to bulk diffusion. Raj proposed a model of cavitation initiation [45]. The time required for initiating a stable cavity was shown to be inversely proportional to the power four or five of the stress around the cavity. The critical radius was given by: $r_c = 2\gamma_s / \sigma_n \sim 1\text{nm}$ ($\gamma_s \sim 1\text{J/m}^2$, $\sigma_n \sim 8$ times the macroscopic stress if $r < h/10$ and $h = 50\text{nm}$). Following our results, localization would accelerate cavity nucleation by a factor higher than 1000.

5. Conclusion

Slip localization is often observed in metallic polycrystals after cyclic deformation (persistent slip bands) or pre-irradiation followed by tensile deformation (channels). To evaluate its effect on crack initiation, crystalline finite element (FE) computations are carried out using microstructure inputs (slip band aspect ratio/spacing). Surface slip bands (low critical resolved shear stress) are embedded in a matrix or small aggregates (high CRSS). The following results are obtained concerning slip and grain boundary stress concentration:

- strong effect of slip band aspect ratio, matrix CRSS and neighbour grains
- weak effect of slip band CRSS and spacing as well as grain boundary angle
- analytical formulae are proposed to predict surface/bulk slips

Finally, the induced surface strain and grain boundary stress concentrations lead to strong accelerations of crack initiation mechanisms whatever the mechanism (surface oxide / grain boundary brittle fracture, vacancy cavity nucleation).

References

- [1] J.V. Sharp, *Phil. Mag.* 16 (1967) 77.
- [2] D.J. Edwards, B.N. Singh, J.B. Bikde-Sorensen, *J. Nucl. Mat.* 342 (2005) 164.
- [3] Z. Jiao, J.T. Busby, G.S. Was, *J. Nucl. Mater.* 361 (2007) 218.
- [4] T.S. Byun, N. Hashimoto, K. Farrell, *J. Nucl. Mat.* 351 (2006) 303.
- [5] P. Lukas, M. Knesnil, J. Krejci, *Phys. Stat. Sol.* 27 (1968) 545.
- [6] J.M. Finney, C. Laird, *Phil. Mag.* 31 (1975) 339.
- [7] Ch. Blochwitz, U. Veit, *Crystal Res. & Technol.* 17 (1982) 529.
- [8] L.C. Lim, R. Raj, *Acta Metall.* 32 (1984) 1183.
- [9] J. Man, K. Obrtlík, Ch. Blochwitz, J. Polak, *Acta Mat.* 50 (2002) 3767.
- [10] C. Wejdemann, O.B. Pedersen, *Mat. Sci. Eng. A* 387 (2004) 556.
- [11] E.H. Lee, M.H. Yoo, T.S. Byun, J.D. Hunn, K. Farrell, L.K. Mansur, *Acta Mater.* 49 (2001) 3277.
- [12] V. Gerold, *Scripta Metall.* 16 (1982) 405.
- [13] K.V. Rasmussen, O.B. Pedersen, *Acta Met.* 14 (1980) 1467.
- [14] J.D. Eshelby, *Proc. R. Soc. Lond. A* 241 (1957) 76.
- [15] E.A. Repetto, M. Ortiz, *Acta Mater.* 45 (1997) 2577.

- [16] M. Sauzay, P. Gilormini, Th. Appl. Fract. Mech. 2002; 38:53.
- [17] M. Sauzay, Ch. Caës, M. Mottot, Ch. Robertson, J. Phys. IV 106 (2003) 99.
- [18] W. Liu, M. Bayerlein, H. Mughrabi, A. Day, P.N. Quedstedt, Acta Metall. Mater. 40 (1992) 1763.
- [19] L.C. Lim, R. Raj, Acta Metall. 32 (1984) 1177.
- [20] E.P. Simonen, S.M. Bruemmer. In: A.R. McIlree, S.M. Bruemmer (Eds). Seventh International Symposium on Environmental Degradation of Materials in Nuclear Power Systems – Water Reactors: National Association of Corrosion Engineers, Houston, TX, 1995, vol. 2 pp.1.
- [21] A. Toivonen, U. Ehrnsten, W. Karlsen, P. Aaltonen, J.-P. Massoud, J.-M. Boursier. In: T.R. Allen, P.J. King, L. Nelson (Eds). 12th Int. Symposium on Environmental Degradation of Materials in Nuclear Power Systems/Water Reactors: The Minerals, Metals & Materials Society, 2005, pp.327.
- [22] S.M. Bruemmer, E.P. Simonen, P.M. Scott, P.L. Andresen, G.S. Was, J.L. Nelson, J. Nucl. Mat. 274 (1999) 299.
- [23] H. Margolin, M.S. Stanescu, Acta Met. 23 (1975) 1411.
- [24] P. Neumann, Scripta Met. Mater. 26 (1992) 1535.
- [25] O. Diard, S. Leclercq, G. Rousselier, G. Cailletaud, Int. J. Plast. 21 (2005) 691.
- [26] A.N. Stroh, Adv. Phys. 6 (1957) 418.
- [27] K. Tanaka, T. Mura, J. appl. Mech. 103 (1981) 97.
- [28] T. Tabata, H. Fujita, M.-A. Hiraoka, K. Onishi. Phil. Mag. A 47 (1983) 841.
- [29] F. Onimus, I. Monnet, J.-L. Béchade, C. Prioul, Ph. Pilvin. J. Nucl. Mater. 328 (2004) 165.
- [30] F.A. Mc Clintock, A.S. Argon. Mechanical behaviour of materials, Addison-Wesley Publishing Company, 1966.
- [31] L. Anand, S. Balasubramanian, K. Kothari. In: Ch. Teodosiu (Ed.). CISM courses n°376, Large plastic deformation of crystalline aggregates, 1996.
- [32] G. Cailletaud, V. Doquet, A. Pineau. In: K. Kussmaul, D. McDiarmid, D. Socie (Eds). Proceedings of Fatigue under Biaxial and Multiaxial Loading, ESIS10, Mechanical Engineering Publications, London, 1991, pp. 131.
- [33] S. Héraud, PhD thesis, Ecole Polytechnique, Palaiseau, France, 1998.
- [34] Y. Li, C. Laird, Mat. Sci. Eng. A 186 (1994) 65.
- [35] C. Gorlier, PhD thesis, Ecole des Mines de Saint-Etienne, France, 2008.
- [36] D.J. Bacon, Y.N. Osetsky, Mat. Sci. Eng. A 400-401 (2005) 353.
- [37] C. Pokor, Y. Brechet, Ph. Dubuisson, J.-P. Massoud, X. Averty, J. Nucl. Mater. 326 (2004) 19.
- [38] Th. Nogaret, Ch. Robertson, D. Rodney, Phil. Mag. 87 (2007) 945.
- [39] <http://www-cast3m cea.fr>
- [40] M. Sauzay, Th. Jourdan, Int. J. Fract. 141 (2006) 431.
- [41] M. Sauzay, Acta Mater. 55 (2007) 1193.
- [42] F.P. Ford, Corrosion 52 (1996) 375.
- [43] A. Van der Ven A, G. Ceder, Acta Mater. 52 (2004) 1223.
- [44] T. Onchi, K. Dohi, N. Soneda, J.R. Cowan, R.J. Scowen, M.L. Castano, J. Nucl. Mater. 320 (2003) 194.
- [45] R. Raj, Acta Metall. 26 (1978) 995.